AIAA 2007-4427

Numerical Investigations of Injection Slot Size Effect on the Performance of Co-Flow Jet Airfoil

Baoyuan Wang[*] Bahaa Haddoukessouni[†] Jonathan Levy[‡] Ge-Cheng Zha[§]
Dept. of Mechanical and Aerospace Engineering
University of Miami
Coral Gables, Florida 33124
E-mail: gzha@miami.edu

Abstract

Three co-flow jet (CFJ) airfoils with injection slot size differed by two times consecutively are calculated by using a RANS CFD solver with 1-equation Spalart-Allmaras model. At the same angle of attack(AoA), the twice larger injection slot size airfoil passes about twice larger jet mass flow rate with the momentum coefficients also nearly doubled. The CFJ airfoil with the largest slot size has the least stall angle of attack(AoA). When the injection slot size is reduced by half, the stall AoA and the maximum lift coefficient is increased. However, when the injection slot size is further reduced by half, the stall AoA is still increased, but the maximum lift coefficient is lower due to the smaller momentum coefficient. The trend of the stall AoA and maximum lift agree with the experiment. At low AoA, both the computed lift and drag agree fairly well with the experiment. At high AoA, both the lift and drag are underpredicted. The reason may be that the RANS model can not handle the turbulence mixing well at high AoA.

1 Introduction

To improve aircraft performance, revolutionary technology should be pursued to dramatically reduce the weight and fuel consumption of the aircraft and to significantly increase aircraft mission payload and stall margin. Both military and commercial aircraft will benefit from this technology. Flow control (FC) is the most promising route to bring significant

[*] Graduate Student
[†] Visiting Senior Undergraduate Student,MATMECA,France
[‡] Visiting Senior Undergraduate Student,MATMECA,France
[§] Associate Professor, AIAA Member

performance improvement to aircraft[1, 2, 3, 4, 5, 6, 7]. Recently, Zha el al. have developed a new promising airfoil flow control technique using a co-flow jet [8, 9, 10, 11], which significantly increases lift, stall margin, and drag reduction.

The co-flow jet airfoil is designed with an injection slot near leading edge and a suction slot near trailing edge on the airfoil suction surface. The slots are opened by translating a large portion of the suction surface downward. A high energy jet is injected tangentially near the leading edge and the same amount of mass flow is drawn in near trailing edge. The turbulent shear layer between the main flow and the jet causes strong turbulence diffusion and mixing under the severe adverse pressure gradient, which enhances lateral transport of energy from the jet to the main flow and allows the main flow to overcome the severe adverse pressure gradient and remain attached at high angle of attack(AoA). The high energy jet induces high circulation and hence generates high lift. The energized main flow fills the wake and therefore reduces drag. The CFJ airfoil can recirculate the jet mass flow and can significantly reduce the penalty to the propulsion system by avoiding dumping the jet mass flow, or having zero net jet mass flow.

The CFJ airfoil concept is in its infant stage and many issues of the working mechanism are not yet well understood. The turbulent mixing between the jet and the main flow that transfers energy from the jet to the main flow is the fundamental working principle[12]. The CFJ airfoil performance is more sensitive to the injection process than to the suction process. The injection slot should be located as close to the leading edge as possible, but should be located downstream of the suction peak. This is to ensure that the adverse pressure gradient after the suction peak enhances the wall jet mixing with the main flow.

In [13], the CFJ airfoils with twice different slot sizes are tested to compare the performance. It is observed that the larger slot size is more effective to reduce drag. The thin slot size airfoil is more energy efficient to increase lift.

The objective of this paper is to simulate the slot size effect on the performance of CFJ airfoils using CFD and compare with the experiment. It is relatively easier to change geometry in CFD simulation than wind tunnel tests to explore different geometries. Three co-flow jet (CFJ) airfoils with injection slot size differed by two times consecutively are studied by using a 3D RANS CFD solver. When the injection total pressures are about the same, the twice larger injection area will allow about twice greater injection mass flow rate as well as the momentum coefficients, which will affect the performance of the CFJ airfoils. The ultimate goal is to find the pattern of optimum geometry configuration for CFJ airfoils.

2 CFJ Airfoil Geometry

Fig.1 shows the baseline airfoil, NACA0025, and three airfoils with co-flow jet slots. The chord length of the airfoil is 0.1527m and the span is 0.3m. The co-flow jet airfoils are defined using the following convention: CFJ4dig-INJ-SUC, where 4dig is the same as NACA 4 digit convention, INJ is replaced by the percentage of the injection slot size to the chord length and SUC is replaced by the percentage of the suction slot size to the chord length. For example, the CFJ0025-065-196 airfoil has an injection slot height of 0.65% of the chord

and a suction slot height of 1.96% of the chord. The suction surface shape is a downward translation of the portion of the original suction surface between the injection and suction slot. The injection and suction slot are located at 7.11% and 83.18% of the chord from the leading edge. The slot faces are normal to the suction surface to make the jet tangential to the main flow.

The CFJ0025-131-196 airfoil is designed with an injection slot size twice than that of the CFJ0025-065-196 airfoil to examine the effect of injection slot size. The suction slot size is unchanged. The slot locations are also the same as those of CFJ0025-065-196 airfoil.

This paper simulates a new CFJ airfoil, CFJ0025-033-065, for which both the injection and suction size is half of the CFJ0025-065-196 airfoil. In other words, for the three CFJ airfoils shown in Fig. 1, the injection slot size are differed by two times consecutively. The purpose is to study the injection geometry effect on the CFJ airfoil performance.

The baseline airfoil, CFJ0025-065-196 airfoil, and the CFJ0025-131-196 airfoil are tested in the wind tunnel tests[13].

3 CFD Solver

The in house CFD software,RANS3D, is used in this research to design the internal ducts and examine the 3D flow field before the wind tunnel tests. The mean flow governing equations are the Reynolds averaged 3D compressible Navier-Stokes equations coupled with the S-A one equation turbulence model[14]. In generalized coordinate system, the conservative form of the equations is given as the following:

$$\frac{\partial Q}{\partial t}+\frac{\partial \mathbf{E}}{\partial \xi}+\frac{\partial \mathbf{F}}{\partial \eta}+\frac{\partial \mathbf{G}}{\partial \zeta}=\frac{1}{Re}\left(\frac{\partial \mathbf{R}}{\partial \xi}+\frac{\partial \mathbf{S}}{\partial \eta}+\frac{\partial \mathbf{T}}{\partial \zeta}+\mathbf{D}\right) \tag{1}$$

In the above equations,

$$Q=\frac{1}{J}\begin{bmatrix}\rho\\ \rho u\\ \rho v\\ \rho w\\ \rho e\\ \rho\tilde{\nu}\end{bmatrix} \tag{2}$$

$$\mathbf{E}=\begin{bmatrix}\rho U\\ \rho uU+l_x p\\ \rho vU+l_y p\\ \rho wU+l_z p\\ (\rho e+p)U-l_t p\\ \rho\tilde{\nu}U\end{bmatrix},\ \mathbf{F}=\begin{bmatrix}\rho V\\ \rho uV+m_x p\\ \rho vV+m_y p\\ \rho wV+m_z p\\ (\rho e+p)V-m_t p\\ \rho\tilde{\nu}V\end{bmatrix},\ \mathbf{G}=\begin{bmatrix}\rho W\\ \rho uW+n_x p\\ \rho vW+n_y p\\ \rho wW+n_z p\\ (\rho e+p)W-n_t p\\ \rho\tilde{\nu}W\end{bmatrix} \tag{3}$$

$$\mathbf{R}=\begin{bmatrix} 0 \\ l_k\tau_{xk} \\ l_k\tau_{yk} \\ l_k\tau_{zk} \\ l_k\beta_k \\ \frac{\rho}{\sigma}\left(\nu+\tilde{\nu}\right)\left(\mathbf{l}\bullet\nabla\tilde{\nu}\right) \end{bmatrix},\ \mathbf{S}=\begin{bmatrix} 0 \\ m_k\tau_{xk} \\ m_k\tau_{yk} \\ m_k\tau_{zk} \\ m_k\beta_k \\ \frac{\rho}{\sigma}\left(\nu+\tilde{\nu}\right)\left(\mathbf{m}\bullet\nabla\tilde{\nu}\right) \end{bmatrix},\ \mathbf{T}=\begin{bmatrix} 0 \\ n_k\tau_{xk} \\ n_k\tau_{yk} \\ n_k\tau_{zk} \\ n_k\beta_k \\ \frac{\rho}{\sigma}\left(\nu+\tilde{\nu}\right)\left(\mathbf{n}\bullet\nabla\tilde{\nu}\right) \end{bmatrix} \tag{4}$$

$$D=\frac{1}{J}\begin{bmatrix} 0 \\ 0 \\ 0 \\ 0 \\ 0 \\ S_\nu \end{bmatrix} \tag{5}$$

where

$$\beta_k=u_i\tau_{ki}-q_k \tag{6}$$

$$\begin{aligned} S_\nu=&\rho C_{b1}\left(1-f_{t2}\right)\tilde{S}\tilde{\nu}+\tfrac{1}{Re}\left[-\rho\left(C_{w1}f_w-\tfrac{C_{b1}}{\kappa^2}f_{t2}\right)\left(\tfrac{\tilde{\nu}}{d}\right)^2\right.\\ &\left.+\tfrac{\rho}{\sigma}C_{b2}\left(\nabla\tilde{\nu}\right)^2-\tfrac{1}{\sigma}\left(\nu+\tilde{\nu}\right)\nabla\tilde{\nu}\bullet\nabla\rho\right]+Re\left[\rho f_{t1}\left(\Delta U\right)^2\right] \end{aligned} \tag{7}$$

In equations above, U, V and W are the contravariant velocities in ξ, η and ζ directions.

$$\begin{aligned} U&=l_t+\mathbf{l}\bullet\mathbf{V}=l_t+l_xu+l_yv+l_zw\\ V&=m_t+\mathbf{m}\bullet\mathbf{V}=m_t+m_xu+m_yv+m_zw\\ W&=n_t+\mathbf{n}\bullet\mathbf{V}=n_t+n_xu+n_yv+n_zw \end{aligned} \tag{8}$$

where $\mathbf{V}=(u,v,w)$ is the velocity vector, $\mathbf{l}$, $\mathbf{m}$, $\mathbf{n}$ are the normal vectors on ξ,η,ζ surfaces with their magnitudes equal to the elemental surface area and pointing to the directions of increasing ξ,η,ζ.

$$\mathbf{l}=\frac{\nabla\xi}{J}\mathrm{d}\eta\mathrm{d}\zeta,\ \mathbf{m}=\frac{\nabla\eta}{J}\mathrm{d}\xi\mathrm{d}\zeta,\ \mathbf{n}=\frac{\nabla\zeta}{J}\mathrm{d}\xi\mathrm{d}\eta \tag{9}$$

l_t, m_t, n_t stand for the grid moving velocities and are defined as

$$l_t=\frac{\xi_t}{J}\mathrm{d}\eta\mathrm{d}\zeta,\ m_t=\frac{\eta_t}{J}\mathrm{d}\xi\mathrm{d}\zeta,\ n_t=\frac{\zeta_t}{J}\mathrm{d}\xi\mathrm{d}\eta \tag{10}$$

When the grid is stationary, $l_t=m_t=z_t=0$.

Since $\Delta\xi=\Delta\eta=\Delta\zeta=1$ in the current discretization, Eqs.(9) and (10) are written as the following in the solver,

$$\mathbf{l}=\frac{\nabla\xi}{J},\ \mathbf{m}=\frac{\nabla\eta}{J},\ \mathbf{n}=\frac{\nabla\zeta}{J} \tag{11}$$

$$l_t = \frac{\xi_t}{J},\ m_t = \frac{\eta_t}{J},\ n_t = \frac{\zeta_t}{J} \tag{12}$$

The shear-stress τ_{ik} and total heat flux q_k in Cartesian Coordinate can be expressed as

$$\tau_{ik} = (\mu + \mu_t)\left[\left(\frac{\partial u_i}{\partial x_k} + \frac{\partial u_k}{\partial x_i}\right) - \frac{2}{3}\delta_{ik}\frac{\partial u_j}{\partial x_j}\right] \tag{13}$$

$$q_k = -\left(\frac{\mu}{Pr} + \frac{\mu_t}{Pr_t}\right)\frac{\partial T}{\partial x_k} \tag{14}$$

where, Pr is the Prandtl number, Pr_t is the turbulent prandtl number, μ is the molecular viscosity determined by Sutherland law and μ_t is the turbulent viscosity determined by S-A model,

$$\mu_t = \rho\tilde{\nu} f_{v1} \tag{15}$$

In eq.(4), (6), (13) and (14), the repeated subscripts i or k represent the coordinates x, y and z following Einstein summation convention. Eq.(13) and (14) are transformed to generalized coordinate system in computation.

The sixth equation of the governing equations is the Spalart-Allmaras(S-A) one equation turbulence model[14]. The functions in the equation are given by

$$\begin{array}{l} f_{v1} = \frac{\chi^3}{\chi^3 + C_{\nu 1}^3},\ \chi = \frac{\tilde{\nu}}{\nu} \\ \tilde{S} = S + \frac{\tilde{\nu}}{Re\kappa^2 d^2} f_{v2},\ f_{v2} = 1 - \frac{\chi}{1+\chi f_{v1}} \\ f_w = g\left[\frac{1+C_{w3}^6}{g^6 + C_{w3}^6}\right]^{\frac{1}{6}},\ g = r + C_{w2}\left(r^6 - r\right),\ r = \frac{\tilde{\nu}}{Re\tilde{S}\kappa^2 d^2} \\ f_{t1} = C_{t1} g_t exp\left[-C_{t2}\frac{\omega_t^2}{\Delta U^2}\left(d^2 + g_t^2 d_t^2\right)\right],\ g_t = min\left(0.1, \frac{\Delta U}{\omega_t \Delta x_t}\right) \\ f_{t2} = C_{t3} exp\left(-C_{t4}\chi^2\right) \end{array} \tag{16}$$

where,$S = \sqrt{\left(\frac{\partial w}{\partial y} - \frac{\partial v}{\partial z}\right)^2 + \left(\frac{\partial u}{\partial z} - \frac{\partial w}{\partial x}\right)^2 + \left(\frac{\partial v}{\partial x} - \frac{\partial u}{\partial y}\right)^2}$ is the magnitude of vorticity which also is transformed to generalized coordinate system, ω_t is the wall vorticity at the wall boundary layer trip location, d is the distance to the closest wall. d_t is the distance of the field point to the trip location, ΔU is the difference of the velocities between the field point and the trip location, Δx_t is the grid spacing along the wall at the trip location.

The constants in S-A model are set to have the values as the following

$$\begin{array}{l} \sigma = \frac{2}{3},\ C_{b1} = 0.1355,\ C_{b2} = 0.622,\ \kappa = 0.41,\ C_{v1} = 7.1, \\ C_{w1} = C_{b1}/\kappa^2 + \left(1 + C_{b2}\right)/\sigma,\ C_{w2} = 0.3,\ C_{w3} = 2, \\ C_{t1} = 1,\ C_{t2} = 2,\ C_{t3} = 1.2,\ C_{t4} = 0.5 \end{array}$$

The finite volume method and Roe scheme[15] is used to discretize the governing equations for steady state solution. To achieve high convergence rate, the implicit time marching scheme is used with the unfactored Gauss-Seidel line relaxation.

The full turbulent boundary layer assumption is used in the computation by setting $C_{t1} = 0$ and $C_{t3} = 0$ in order to be consistent with the tripped boundary layer in the experiments. Since CFD solutions are obtained from the steady state calculations based on RANS model, the unsteady details of the shear layer mixing entrainment and large coherent vortex structures are not able to be captured. The total pressure and total temperature are given at the injection duct inlet as the boundary conditions.

3.1 Jet Effects on CFJ Aircraft Performance

By using a control volume analysis, Zha et al. derived an expression for the force effect of the injection and suction jets on the CFJ wing [9]. In keeping with Newton's third law, at the injection and suction slots, the high velocity flow produces a reactive force which must be taken into account in the drag and lift calculations. The expressions for these reaction forces are given as:

$$F_{x_{cfj}} = (\dot{m}_j V_{j1} + (p_{pj1} A_{j1}) * cos(\theta_1 - \alpha) - \gamma(\dot{m}_j V_{j2} + (p_{j2} A_{j2}) * cos(\theta_2 + \alpha) \tag{17}$$

$$F_{y_{cfj}} = (\dot{m}_j V_{j1} + (p_{pj1} A_{j1}) * sin(\theta_1 - \alpha) - \gamma(\dot{m}_j V_{j2} + (p_{j2} A_{j2}) * sin(\theta_2 + \alpha) \tag{18}$$

Where the subscripts 1 and 2 refer to the injection and suction respectively and θ_1 and θ_2 are the angles that the injection and suction slots, respectively, make to the vertical. The total modified lift and drag on the wing can then be expressed as:

$$D = R'_x - F_{x_{cfj}} \tag{19}$$

$$L = R'_y - F_{y_{cfj}} \tag{20}$$

These quantities modify the forces calculated from the surface integral, R'_x and R'_y, in order to correct for the reaction forces induced by the jet effect. It is expected, as can be seen from equations 17 and 18, that the corrected Lift will decrease when $v_{j1} > 0$ and increase when $v_{j1} < 0$.

4 Results and Discussion

The chord length of the airfoil is 0.1527m and the freestream Mach number is about 0.11. This gives the Reynolds number about 3.8×10^5, which is in the laminar/transitional region. To make the boundary layer fully turbulent in order to mimic the realistic flight conditions, the airfoil leading edge is tripped to trigger the turbulence in the wind tunnel tests. In CFD simulation, the boundary layer is assumed to be fully turbulent starting from the leading edge. The different boundary conditions between the experiment and CFD is that the CFD simulates the airfoil in an open field with no wind tunnel wall.

To study the effect only caused by the geometry, the injection total pressure is iterated to match the experimental momentum coefficient. The static pressure at the suction duct entrance is iterated to match the injection jet mass flow rate.

A typical 2D computational mesh is shown in Fig. 2. The mesh has total 25536 cells.

Fig. 3 is the momentum coefficient while the AoA is varied. In the wind tunnel experiment, the injection total pressure coefficients for the CFJ0025-065-196 and CFJ0025-131-196 are the same. Since the injection slot size is differed by two times, the mass flow rate and the momentum coefficients are also about two times different as shown in Fig. 3. The CFD computation matches the experimental momentum coefficients very well. For the CFJ0025-033-065 airfoil created in this paper, since no experiment is done, the momentum coefficients are determined by using the same injection total pressure as that of the CFJ0025-065-196 airfoil, which generates about half of the momentum coefficients of the CFJ0025-065-196 airfoil.

Fig.4 is the lift coefficient comparison for the airfoils with the different slot sizes. The experiment shows that the CFJ0025-131-196 airfoil with twice larger slot size and momentum coefficients only generate slightly higher lift than the CFJ0025-065-196 airfoil before it stalls. The stall AoA and the maximum lift of the CFJ0025-131-196 airfoil is even less than that of the CFJ0025-065-196 airfoil. The CFD numerical simulations also generate the same trend. Quantitatively, the computed lift coefficients agree quite well with the experiment before AoA=20°. When the AoA is greater than that, the CFD under-predicts the lift. It may be because that the RANS model can not predict the mixing process well, which is inherently unsteady and may also have large vortex structures generated. The stall AoA is predicted quite well, except that the trend of the stall is more gradual instead of being abrupt as shown in the experiment.

The results of the CFJ0025-065-196 and CFJ0025-131-196 airfoil indicates that the smaller injection airfoil has higher maximum stall AoA and lift. When the injection slot size is further reduced by half as the CFJ0025-033-065 airfoil, the stall AoA is also greater than that of the CFJ0025-065-196 airfoil. However, the maximum lift of the CFJ0025-033-065 airfoil is lower than that of the CFJ0025-065-196 airfoil due to the jet momentum or kinetic energy is lower.

Fig.5 is the drag coefficient of the CFJ airfoils with different injection slot sizes. Similar to the lift prediction, the computed drag agree quite well at low AoA. At high AoA, the drag is significantly under-predicted. Again, this may be attributed to the RANS turbulence model. In the experiment, the larger injection slot airfoil has slightly lower minimum drag, but the computation does not generate such difference.

Fig. 6 is the wake profiles of the baseline NACA0025 airfoil and the three CFJ airfoils one chord length downstream of the airfoil trailing edge. It shows that the baseline NACA0025 airfoil has a the deepest velocity deficit. The CFJ airfoils has shallower wake profiles due to the CFJ energizing the main flow.

Fig. 7 is the surface isentropic Mach number for the airfoils at AoA=20^0. It can be seen that the surface loading, or the circulation, of the CFJ airfoils is much larger than that of the NACA0025 airfoil. The leading edge suction peak Mach number of the CFJ airfoil is

higher and the stagnation point is more downstream with the increase of the slot size. It can be seen that the injection locations are located downstream of the peak Mach number to make use of the adverse pressure gradient to enhance mixing[16].

Fig. 8 to 11 are the Mach number contours with streamlines of the baseline NACA0025 airoil and the three CFJ airfoils at AoA=20° respectively. The baseline airfoil has a massive separation, which is consistent with the experiment[13]. The CFJ0025-033-065 airfoil also experiences a small separation at the trailing since the jet momentum is not strong enough. Both the CFJ0025-065-196 and CFJ0025-131-196 airfoils do not have any separation at AoA=20° due to the stronger CFJ, which is also the same as demonstrated in the wind tunnel tests. It is interesting to note that even though the CFJ0025-033-065 airfoil has the separation at AoA=20° , the airfoil stall does not occur until AoA=50°. The airfoil may work under a dynamically stable flow conditions, which may only be seen if unsteady simulation is conducted.

5 Conclusions

Three co-flow jet (CFJ) airfoils with injection slot size differed by two times consecutively are calculated by using a RANS CFD solver with 1-equation Spalart-Allmaras model. At the same angle of attack(AoA), the twice larger injection slot size airfoil passes about twice larger jet mass flow rate with the momentum coefficients also nearly doubled. However, same as the trend shown in the wind tunnel experiment, the CFJ0025-131-196 airfoil, which has the largest injection slot size, has the smallest stall AoA. The CFJ0025-065-196 airfoil with the injection slot size reduced by half has higher stall AoA and maximum lift coefficient, which is consistent with the experiment. For the CFJ0025-033-065 airfoil, which is created in this paper with the injection slot size further reduced by half of the CFJ0025-065-196 airfoil, the CFD simulation indicates that the stall AoA is further increased, but the maximum lift coefficient is lower due to the relatively weaker CFJ. The predicted lift at AoA lower than 20° and the predicted drag at AoA lower than 10° agree fairly well with the experiment. At high AoA, both the lift and drag are under-predicted, in particular for the drag, which is substantially under-predicted. This may be attributed to the RANS turbulence model which can not capture the inherent unsteady mixing process of the CFJ airfoil.

6 Acknowledgment

This research is supported by ARO/AFOSR Grant 50827-RT-ISP, monitored by Rhett Jefferies(AFOSR) and Jenny Haire (ARO).

References

[1] W. L. I. Sellers, B. A. Singer, and L. D. Leavitt, "Aerodynamics for Revolutionary Air Vehicles." AIAA 2004-3785, June 2003.

[2] M. Gad-el Hak, "Flow Control: The Future ," *Journal of Aircraft*, vol. 38, pp. 402–418, 2001.

[3] M. Gad-el Hak, *Flow Control, Passive, Active, and Reactive Flow Management*. Cambridge University Press, 2000.

[4] S. Anders, W. L. Sellers, and A. Washburn, "Active Flow Control Activities at NASA Langley." AIAA 2004-2623, June 2004.

[5] C. P. Tilmann, R. L. Kimmel, G. Addington, and J. H. Myatt, "Flow Control Research and Application at the AFRL's Air Vehicles Directorate." AIAA 2004-2622, June 2004.

[6] D. Miller, , and G. Addington, "Aerodynamic Flowfield Control Technologies for Highly Integrated Airframe Propulsion Flowpaths." AIAA 2004-2625, June 2004.

[7] V. Kibens and W. W. Bower, "An Overview of Active Flow Control Applications at The Boeing Company." AIAA 2004-2624, June 2004.

[8] Zha, G.-C. and Gao, W., and Paxton, C. and Conley, A., "Effect of Injection Slot Size on the Performance of Coflow Jet Airfoil," *Journal of Aircraft*, vol. 43, pp. 987–995, 2006.

[9] Zha, G.-C. and Paxton, C. and Conley, A., "A Novel Flow Control Method for Airfoil Performance Enhancement Using Co-flow Jet," *Applications of Circulation Control Technologies, AIAA Book Series, Progress in Aeronautics and Astronautics*, vol. 214, pp. 293–314, 2006.

[10] Zha, G.-C., Gao, W. and Paxton, C.D., "Jet Effects on Co-Flow Jet Airfoil Performance," *AIAA Journal*, vol. 45, pp. 1222–1231, 2007.

[11] Zha, G.-C., Bruce F. Carroll, Paxton, C., Clark A. conley and Adam Wells, "High Performance Airfoil Using Co-Flow Jet Flow Control," *To appear in AIAA Journal*, 2007.

[12] G.-C. Zha and C. Paxton, "A Novel Airfoil Circulation Augment Flow Control Method Using Co-Flow Jet." NASA/ONR 2004 Circulation Control Workshop, 16-17 March 2004. AIAA Paper 2004-2208, June 2004.

[13] G.-C. Zha, B. Carroll, C. Paxton, A. Conley, and A. Wells, "High Performance Airfoil with Co-Flow Jet Flow Control." AIAA-2005-1260, 2005.

[14] P. Spalart and S. Allmaras, "A One-equation Turbulence Model for Aerodynamic Flows." AIAA-92-0439, 1992.

[15] P. Roe, "Approximate Riemann Solvers, Parameter Vectors, and Difference Schemes," *Journal of Computational Physics*, vol. 43, pp. 357–372, 1981.

[16] T. C. Greitzer, E.M. and M. Graf, "Internal Flows." Cambridge Univ. Press, Cambridge, England, 2004, 2004.

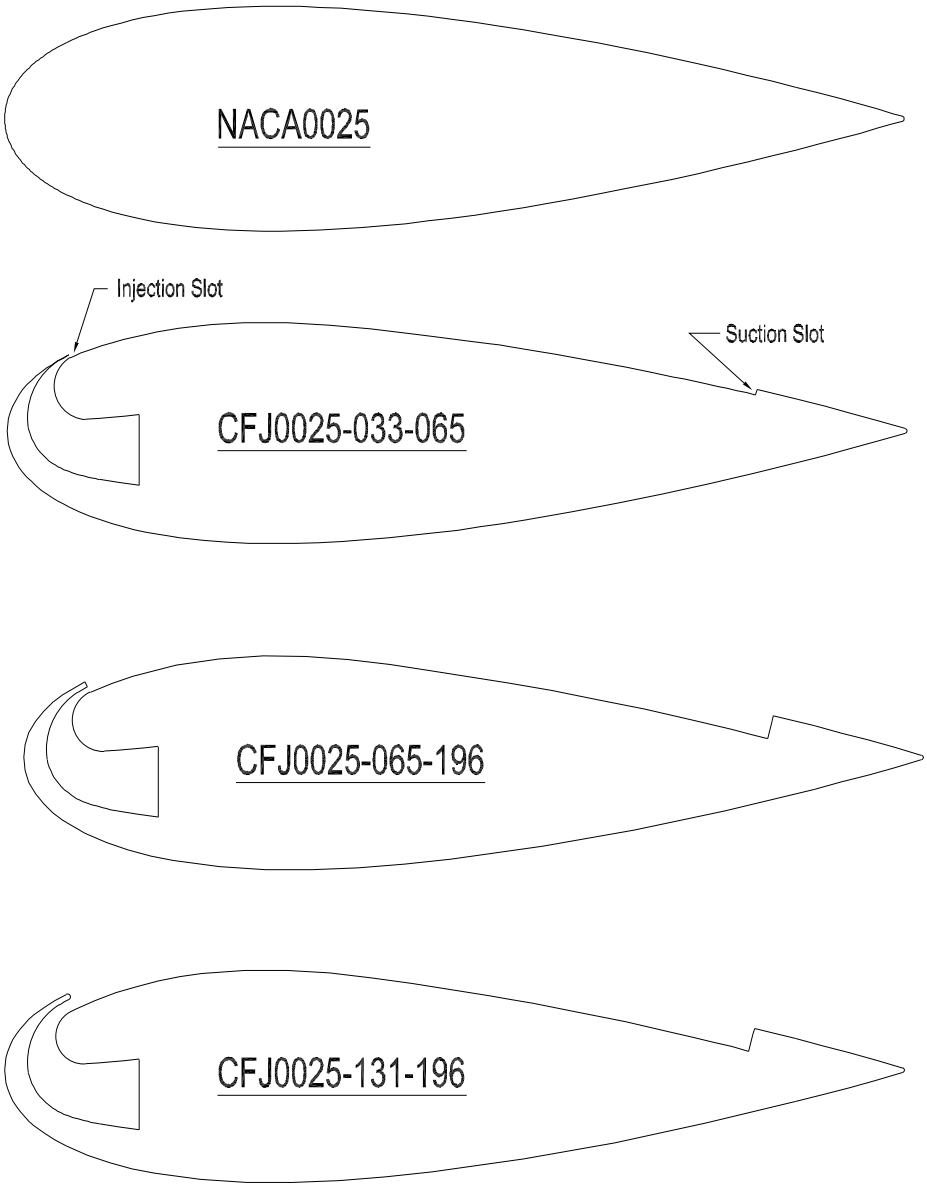

Figure 1: Airfoil section of the baseline airfoil of NACA0025, CFJ airfoil CFJ0025-065-196 and CFJ airfoil CFJ0025-131-196.

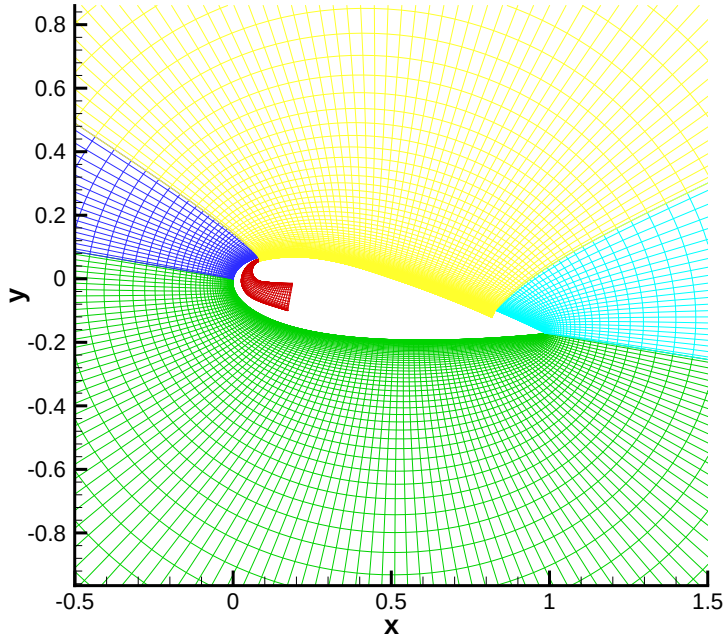

Figure 2: 5-block grids for CFJ airfoil.

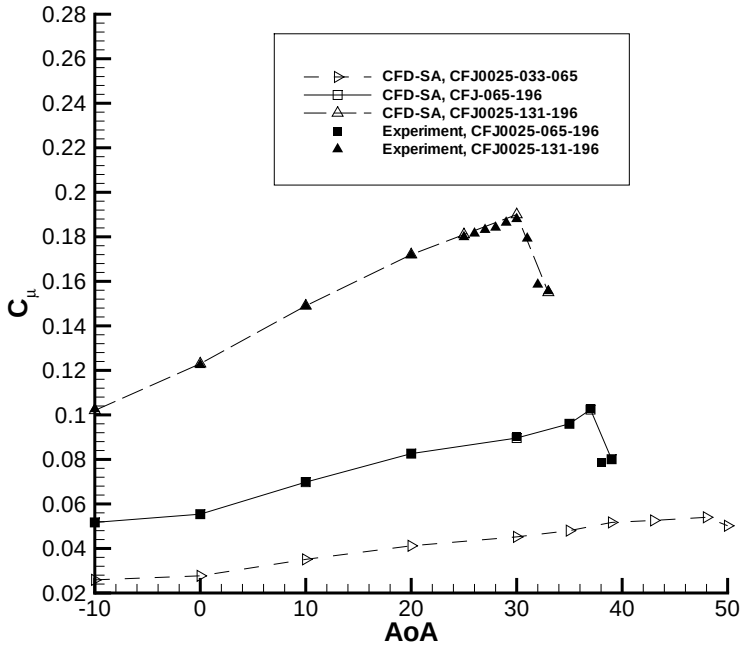

Figure 3: Injection momentum coefficient of CFJ airfoils with Different Injection Slot Size.

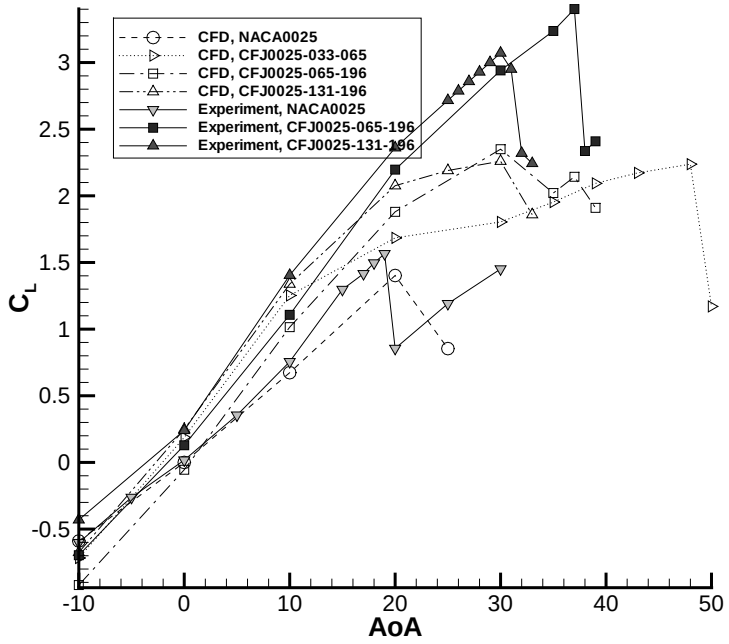

Figure 4: Lift coefficient of CFJ airfoils with Different Injection Slot Size.

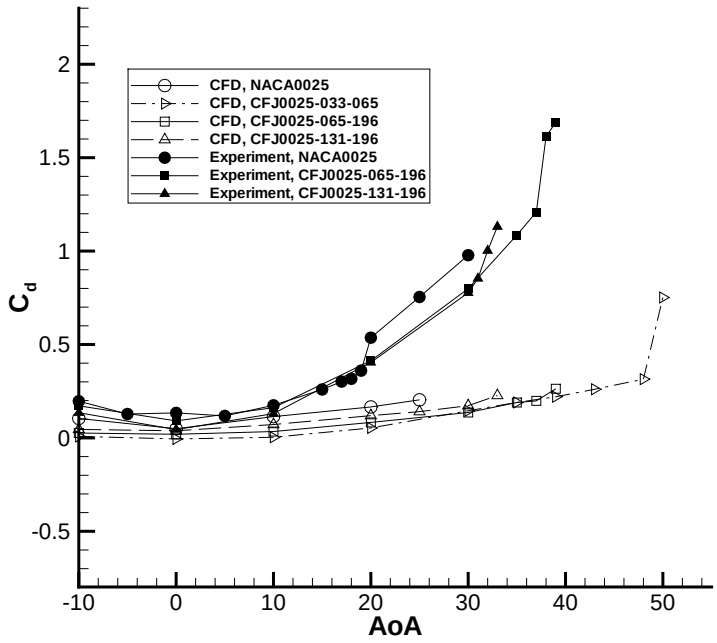

Figure 5: Drag coefficient of CFJ airfoils.

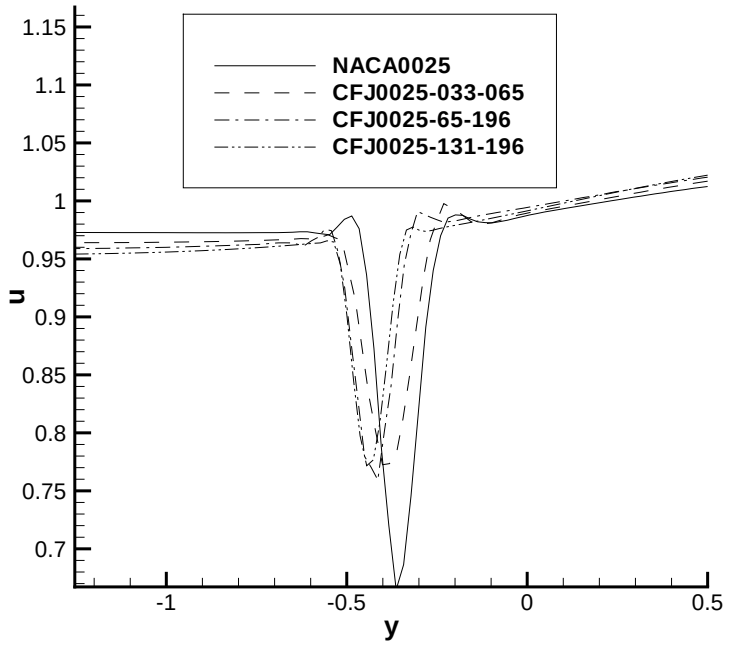

Figure 6: Wake profile of the CFJ airfoil with injection.

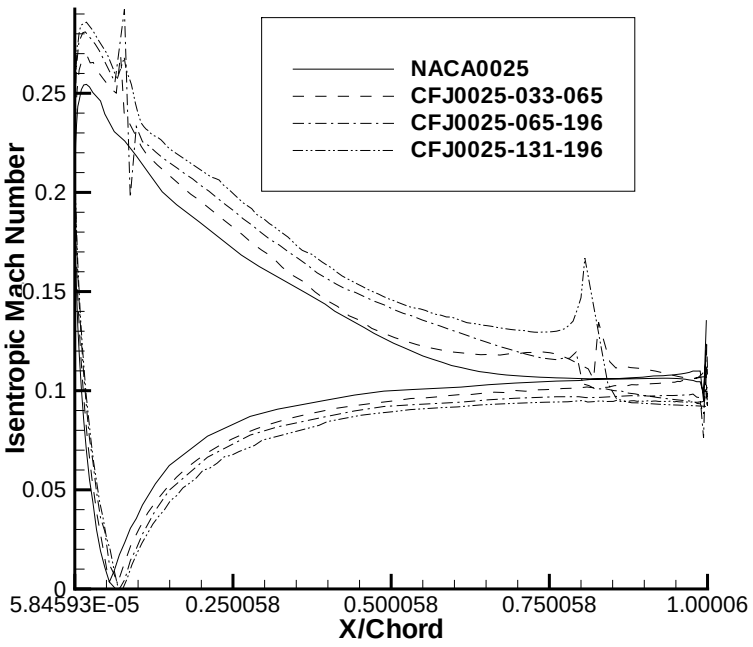

Figure 7: The isentropic Mach number distribution on the surface of the CFJ airfoil with injection.

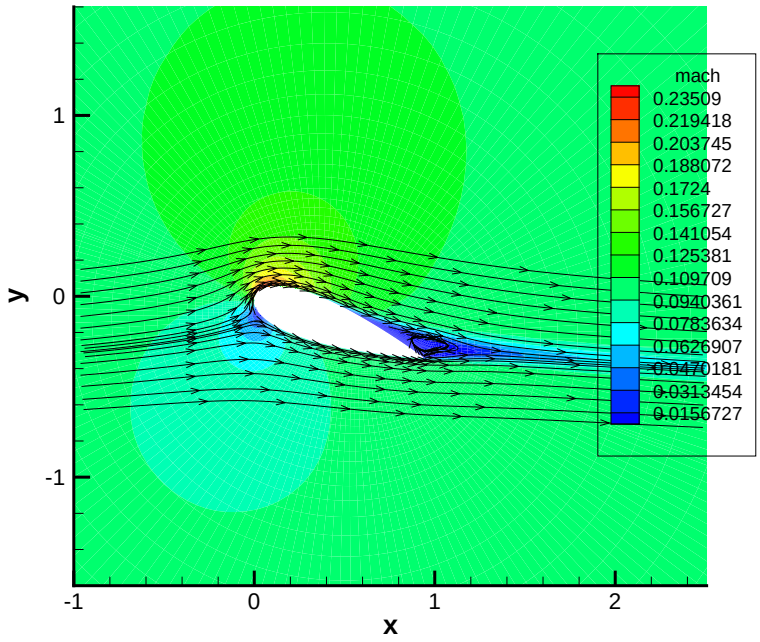

Figure 8: Mach number contours of NACA0025 airfoil at AoA=20°.

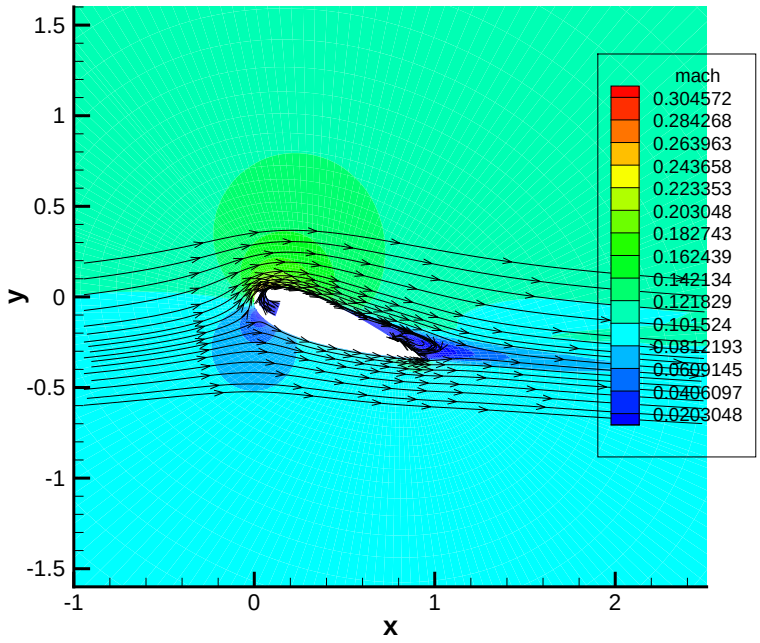

Figure 9: Mach number contours of CFJ0025-033-065 airfoil at AoA=20°.

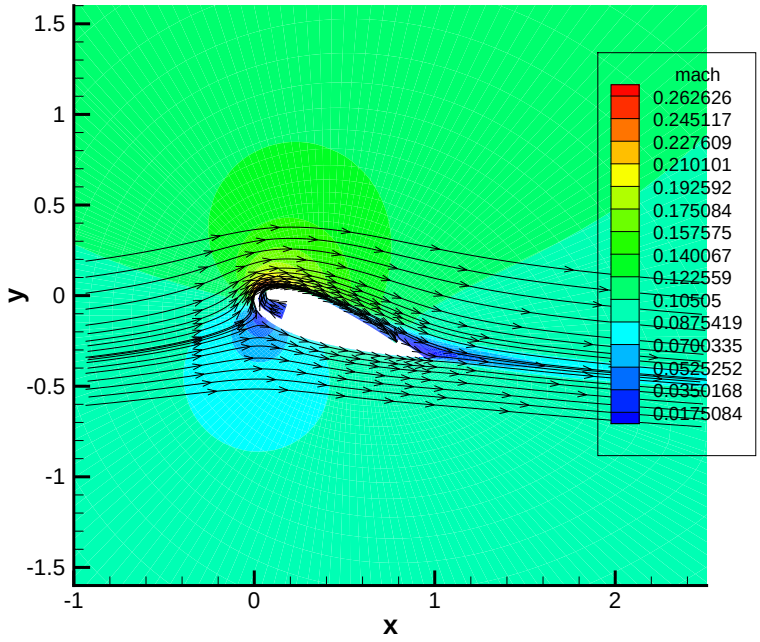

Figure 10: Mach number contours of CFJ0025-065-196 airfoil at AoA=20°.

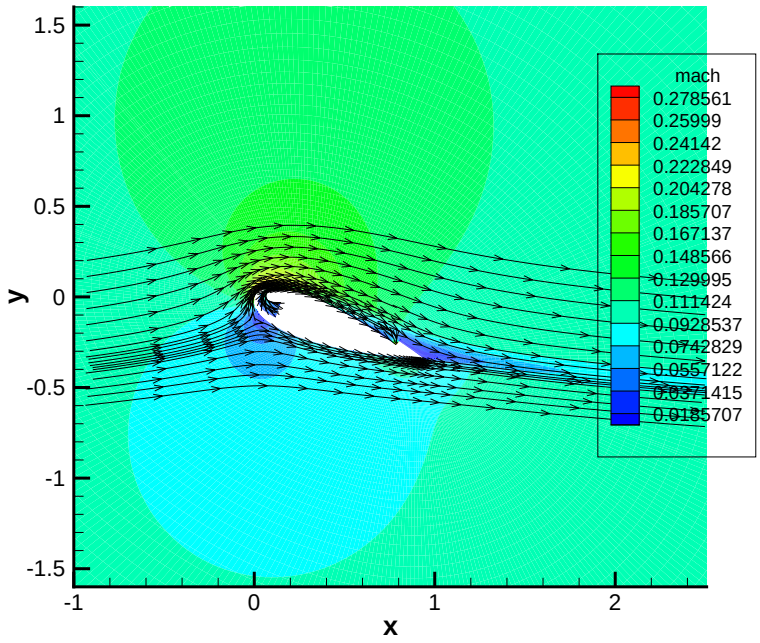

Figure 11: Mach number contours of CFJ0025-131-196 airfoil at AoA=0°.